Wear 268 (2010) 41–49

Contents lists available at ScienceDirect

Wear

journal homepage: www.elsevier.com/locate/wear

Edges, clearances, and wear: Little things that make big differences in bushing friction

Rachel S. Colbert[a], Luis A. Alvarez[a], Matthew A. Hamilton[a], Jason G. Steffens[a], John C. Ziegert[b], David L. Burris[c], W. Gregory Sawyer[a,*]

[a] Department of Mechanical and Aerospace Engineering, University of Florida, United States
[b] Department of Mechanical Engineering, Clemson University, United States
[c] Department of Mechanical Engineering, University of Delaware, United States

ARTICLE INFO

Article history:
Received 6 March 2008
Received in revised form 12 June 2009
Accepted 18 June 2009
Available online 26 June 2009

Keywords:
Wear
Bushing
Solid lubrication
Friction

ABSTRACT

Traditional pin-on-flat tribometers are necessary instruments for making direct measurements of tribological properties, but mechanical design of even simple systems often requires application-specific information that only component level testing can provide. This paper uses the design and operation of a bushing tribometer to elucidate geometric effects that plague bushing systems. For example, the nature of the bushing edge has a dramatic influence on the performance of the system in practice where the system is necessarily over-constrained. It is shown mathematically that the torque requirements increase as the wrap angle of the contact spreads for a constant friction coefficient; at steady state the equation for calculated torque requirement is found. This is demonstrated using ultra-high molecular weight polyethylene bushings that showed increasing torques at decreasing clearances. A polytetrafluoroethylene (PTFE) bushing with 150 μm interference initially required 50% more torque than a PTFE bushing with 350 μm clearance. As the two different bushings ran into steady state wear, the torque asymptotically approached the mathematically derived value. The results of these experiments provide designers insight into the design of successful bushing pairs and the ability to tune frictional torques without changing material through the selection of clearance.

1. Introduction

There are ever increasing applications where traditional fluid lubrication techniques are precluded; solid lubricants are often the only available solution [1,2]. Space applications, for example, present a myriad of design challenges including temperature extremes, near perfect vacuum, and atomic oxygen. As a result, the design engineers are faced with the unenviable task of providing effective and reliable lubrication using sparse empirical data and incomplete knowledge of past successes [2,3].

In bushings, appropriate constraints and degrees of freedom are provided *via* the tribological interface [4,5]. This results in the contact geometries being substantially more complicated than those of general tribology experiments. In the simplest revolute joint, a shaft rotates within the slightly larger journal or bushing. This ubiquitous design is subject to evolutions of geometry, contact area and pressure distribution, which result in a deceptively high degree of complexity and evolution in friction coefficient and torque. Further, during application, variations in temperature and stress results in distortion and misalignment. Engineers frequently desire component level testing for accurate prediction of the joint and mechanism behavior, life, performance, and ultimately failure [3].

This paper reports on the design, construction, and operation of a component-level bushing tribometer that can operate in vacuum and support studies on the effects of bushing geometry and misalignments on torque, friction, and wear. The results provide design engineers with guidelines for the design of bushings.

2. Tribometer design

The basic design concept and primary bushing tribometer components are illustrated in Fig. 1. The most critical requirement of the design is the ability to accurately measure low friction coefficients. The load measurement strategy used here follows the methodology described by Schmitz et al. [6,7]. A six-channel load cell is rigidly mounted to the bushing sample. This design promotes low uncertainty measurement because, as shown in Fig. 2, the loads on the

* Corresponding author at: Department of Mechanical and Aerospace Engineering, University of Florida, 237 Mechanical Engineering Building, Gainesville, FL 32611, United States. Tel.: +1 352 392 8488.
E-mail address: wgsawyer@ufl.edu (W.G. Sawyer).

0043-1648/$ – see front matter © 2009 Elsevier B.V. All rights reserved.
doi:10.1016/j.wear.2009.06.030

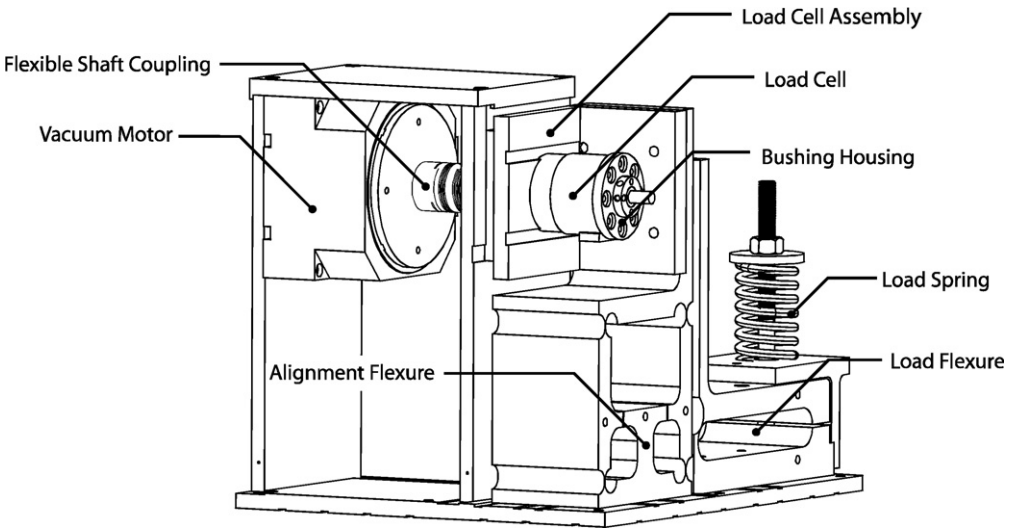

Fig. 1. Schematic illustration of the bushing tribometer; primary components are labeled (vacuum compatible servo-motor, a flexible coupling between the motor and the sample shaft, the six channel strain-gauge based vacuum compatible load cell, a bushing housing, the alignment and load flexures, and a spring used for applying the normal load).

bushing are transmitted directly through the load cell. Further, the stiffness of the multiaxial transducer maintains the spatial orientation of the samples during testing, and there are no kinematic linkages or mechanisms that could confound with the force measurements.

The design requirement for vacuum operation and the vacuum chamber enclosure precluded the use of pneumatics and hydraulics; the large force requirements (500 N) precluded the use of dead weights. Traditionally, spring-based loading systems are uncommon because creep and wear lead to load decay. Soft springs minimize load decay, and since normal loads are continuously recorded, this method was selected for its combination of high load capability, ease of use and compact size.

This spring-based load application mechanism uses elastic flexures for motion. The degrees of freedom are exaggerated and illustrated in Fig. 3. Flexures were chosen over bearings because of the difficulties discussed in Section 1. The spring is compressed and the load arm transmits force to the load cell assembly through an alignment flexure that restricts the load cell assembly to nearly horizontal in-plane motion. Once the test bushing

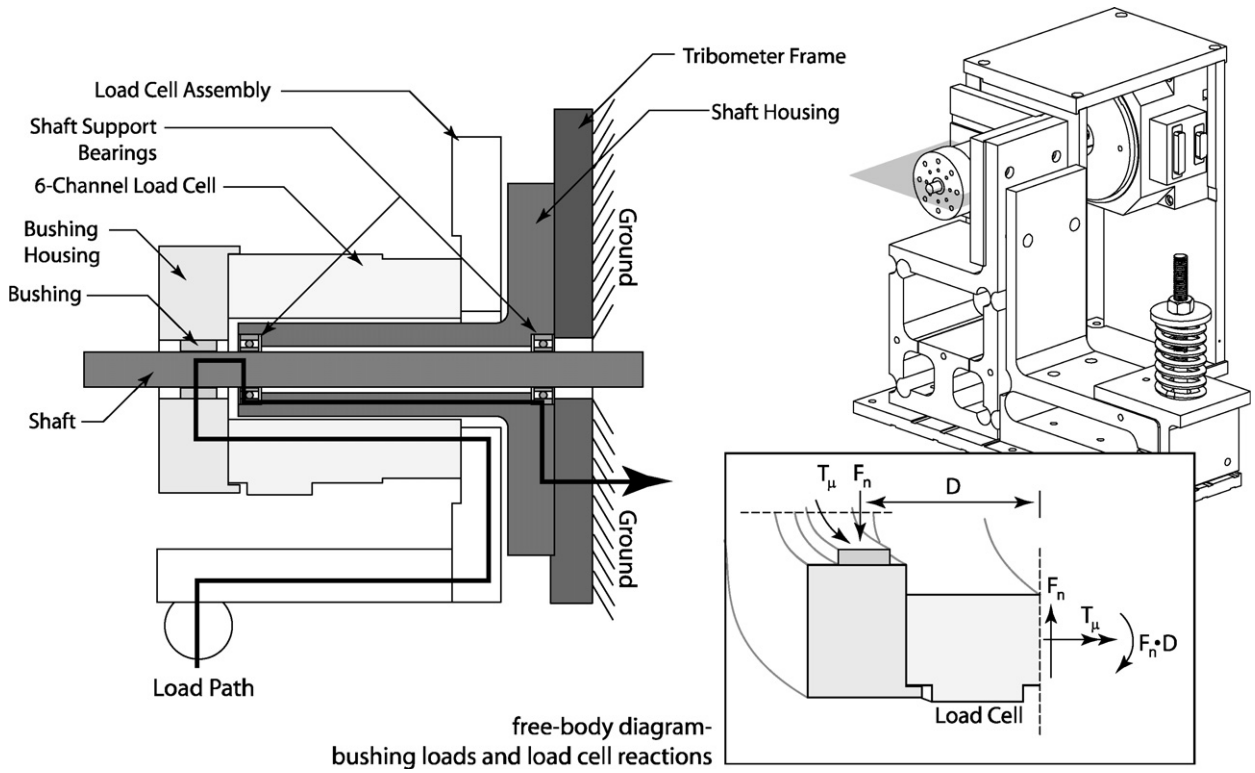

Fig. 2. The load path illustrated in the section view above shows that the entire load applied to the bushing component assembly is transmitted through the six-axis load cell. This ensures that all net forces experienced by the sample are recorded during data collection. The uncertainties associated with the ratio of torques, moment arms, and applied loads are much smaller than the fluctuations observed during operation.

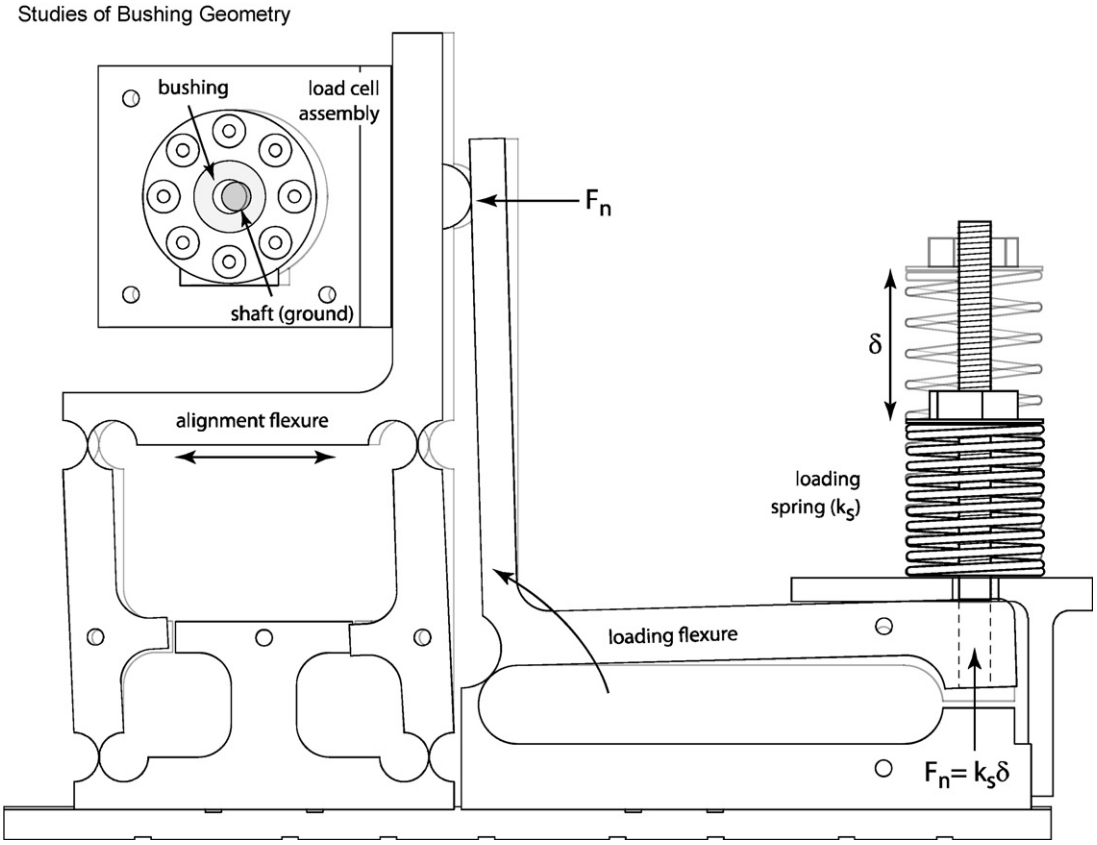

Fig. 3. Schematic illustration of the normal load application mechanism. A load spring is compressed with a drive-nut. The compression force in the spring is reacted by a steel ball mounted to the alignment flexure. The alignment flexure constrains the load cell assembly to horizontal motion. The grounded shaft reacts the applied force and prevents horizontal motion of the load cell assembly.

and shaft are securely mounted, the mechanism is constrained by the bushing/shaft; the shaft and shaft support bearings provide the force path to ground as shown in Fig. 2. Rigid stops on the alignment and loading flexures restrict mobility and prevent overstraining.

The motor and test shaft are both supported by vacuum-compatible grease-lubricated ball-bearings (note: of some interest here the WS_2-coated vacuum-compatible shaft support bearings of the original design failed before the end of the first test and had to be replaced). The servo motor provides rotary motion from 0.001 to 1000 rpm with a maximum torque output of 3 N m. Chilled water is passed into the chamber and circulated through the aluminum motor base to provide cooling to the motor. A helical coupling minimizes the transmission of non-torque loads to the shaft.

As described by Burris and Sawyer [8], the substantial errors that result from even small angular misalignments between the load cell axis and surface normal direction are eliminated when motion reversals are used to subtract the offset. The ratio of torque to the product of normal load and shaft radius is not the friction coefficient but is extremely useful in design. This common parameter is defined here as μ' and is calculated by dividing the subtracted moment by the shaft radius and the magnitude of the vector sum of F_x and F_y in the forward and reverse directions of the motor. The average of the absolute value of μ' in the forward and reverse directions yields the corrected value of μ'.

The entire apparatus is located within a vacuum chamber which allows variable pressure, composition, and temperature of the ambient environment. The base pressure of 10^{-6} Torr is reached in less than 2 h and is used to simulate space conditions. Liquid nitrogen is used to cool a cold finger that is used for temperature control. The system is capable of low uncertainty torque and life measurements in a wide range of application-relevant environments.

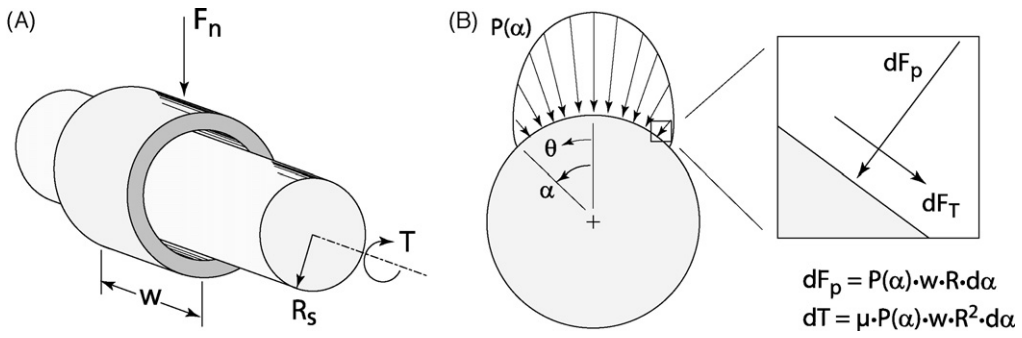

Fig. 4. (A) Illustration of bushing and shaft geometry. (B) Estimated pressure distribution after static loading of a shaft onto a bushing; the application of a torque results in a traction distribution that is equal to the product of the pressure distribution and the friction coefficient.

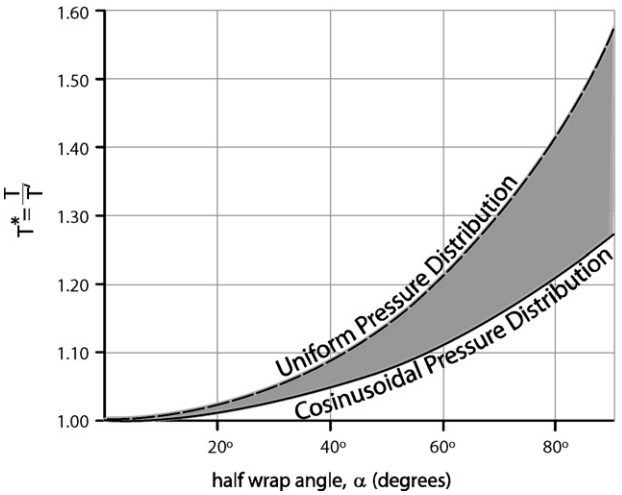

Fig. 5. T^* plotted versus the half wrap angle for uniform and cosinusoidal pressure distributions.

3. Computation of friction coefficient

Friction at the contact interface produces a torque that must be overcome by the drive motor. The magnitude of the frictional torque dictates the motor size, transmission ratios, and power draw; it is therefore of great practical importance during design. Torque requirements (T') are calculated by inserting the friction coefficient (μ) of a material pair of interest into Eq. (1), where F_n is the normal force and R_s is the shaft radius:

$$T' = \mu \cdot F_n \cdot R_s \tag{1}$$

Though useful, we will show that this equation actually underestimates the torque requirement, essentially because this expression treats the contact as a point rather than a distributed area.

A typical bushing system is shown schematically and labeled in Fig. 4A. Upon loading, elastic deformations produce non-uniform pressure distributions (P_θ) as shown in Fig. 4B. Rotation of the shaft results in a distributed traction stress (μP_θ) with a magnitude equal to the product of the friction coefficient and distributed pressure. This traction stress produces torque about the axis of rotation. The normal force (F_n) and torque (T) resultants are found by integrating Eqs. (2) and (3), where α is half the contact wrap angle, θ is the angular coordinate, R_s is the shaft radius and w is the bushing width:

$$F_n = 2\int_0^\alpha P_\theta \cos(\theta) w R_s \, d\theta \tag{2}$$

$$T = 2\int_0^\alpha \mu P_\theta \, w R_s^2 \, d\theta \tag{3}$$

Defining a dimensionless torque $T^* = T/T'$ and inserting Eqs. (2) and (3) into Eq. (1) gives Eq. (4).

$$T^* = \frac{T}{\mu \cdot F_n \cdot R_s} = \frac{2\int_0^\alpha \mu P_\theta \, w R_s^2 \, d\theta}{\mu \cdot R_s \cdot 2\int_0^\alpha P_\theta \cos(\theta) w R_s \, d\theta}$$

$$= \frac{\int_0^\alpha P_\theta \, d\theta}{\int_0^\alpha P_\theta \cos(\theta) \, d\theta} \tag{4}$$

Because there are antagonistic force components of the pressure distribution that do not support the normal force, T^* is always greater than unity; its magnitude depends on the distribution of pressure, and therefore, the material properties, contact geometry, and wear. At $\alpha = \pi/2$, a constant pressure distribution results in $T^* = \pi/2 \simeq 1.57$. In the limiting case of steady state wear, it is shown in Appendix A that the pressure becomes a cosinusoidal function of the angular coordinate; in this case the half wrap angle is nearly $\alpha = \pi/2$ and $T^* \simeq 1.25$. While the actual pressure distribution is unknown, these are presented as bounding cases (a semi-elliptical distribution lies in between). Fig. 5 shows these bounding cases of T^* as a function of the half wrap angle. It should be noted that the effects of wear debris are neglected here (qualitatively we observe/suspect that debris increases internal pressure and leads to increased torque, this has also been observed and discussed in Mosleh et al. [1]).

Mathematical descriptions of reaction forces and torques as functions of wrap angle are particularly useful when the wrap angle is known or there are mathematical relationships that can provide solutions for the wrap angle as a function of load, geometry, and material parameters [9]. Appendix B outlines a derivation of a Winkler-based model of μ' in terms of the elastic properties of the bushing, normal force and clearance. The results of this modeling is a chart with contour lines of constant μ' over orders of magnitude variations in relevant nondimensional terms that

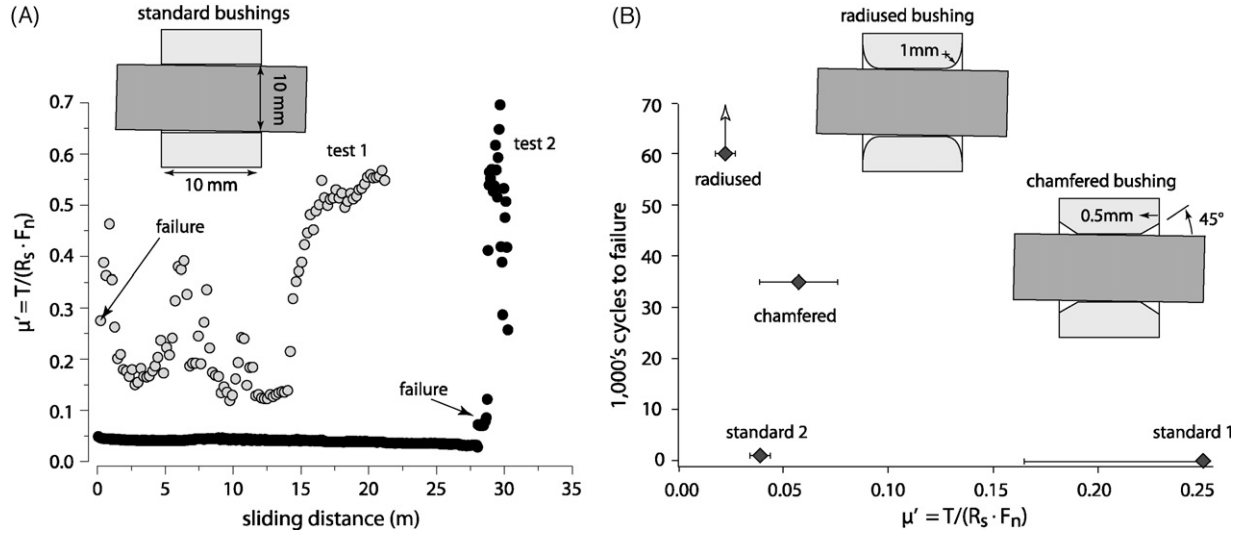

Fig. 6. (A) Friction coefficient (μ') plotted versus sliding distance for two nominally identical standard bushing joints coated with commercially available flight-certified solid lubricant coatings. (B) Thousands of cycles to failure plotted versus friction coefficient (μ') for standard and edge-modified bushings. The contrasting frictional behaviors result from a strong sensitivity to angular misalignment between the bushing and shaft.

can be used to approximate behavior in the absence of empirical data.

4. Description of bushing experiments

Mathematical considerations of the torque generated in bushing contacts indicate that friction measurements based on torques are not fundamental. Further, the modeling suggests that the misalignments and conformal contact geometries found in practice may actually dominate the performance. The studies described here were selected to examine the effects of misalignment and contact geometry independently.

4.1. Variable edge geometry

Three different edge conditions were examined: sharp (standard), chamfered, and radiused. The chamfered bushing had an edge chamfer at 45° for 0.5 mm. The radiused bushing had an edge radius of 1 mm. The shafts were made from 455 stainless steel and were ground to a nominal diameter of 10 mm. The bushings were 10 mm wide and were machined from 440C stainless steel. After machining, the 440C bushings were heat treated to a Rockwell C hardness of 58. The finished bushings were matched with shafts to a clearance of 50 μm ± 5 μm.

A commercially available solid lubricant coating of MoS_2/Au/Sb_2O_3 that had a manufacturer reported thickness of approximately 2 μm was applied to both the shafts and the bushings. Experiments were run under a normal load of 100 N, and a rotary speed of 20 rpm. Because this coating prefers vacuum/inert environments, all experiments were run in vacuum at better than 1×10^{-6} Torr.

4.2. Variable initial clearance

Initial experiments designed to examine the effects of clearance on bushing torque used ultra-high molecular weight polyethylene (UHMWPE) bushings. Like the previously described experiments, the bushings were 10 mm wide, and mated against 455 stainless steel polished shafts. These UHMWPE bushings were CNC machined to clearances of 200, 10, 8, and 3 μm ± 10 μm. The normal load was 400 N and the rotary speed was 20 rpm. UHMWPE was selected because of its ultra-low wear behavior under unidirectional sliding [10,11]. Furthermore, the moderate contact pressures (~4 MPa) ensured that the experiments ran over 7 m of sliding and were essentially devoid of gross geometric changes (*i.e.* the frictional torques were not a function of evolving surface geometry).

4.3. Evolving contact wrap angle

In many systems the initial contact geometry is not the geometry found at steady state [12,13]. Here a high wear material, polytetrafluoroethylene (PTFE), was selected as the bushing material specifically because of the very high wear rates and relative ease with which the samples can be run-in to steady state wear conditions [14,15]. In addition, PTFE is reputed for stable frictional behavior and the evolution in torque behavior can almost wholly be attributed to the geometric evolution due to wear rather than simple frictional variation with sliding distance [16]. Two bushings were prepared: one was machined to an interference of 150 μm while the other had a clearance of 350 μm. The 455 stainless steel shaft was preconditioned with a PTFE transfer film from a sacrificial bushing in order to minimize initial transients. Test samples were run for approximately 70 m to reach steady state wear conditions.

4.4. Zero wrap angle friction measurement

A control experiment was designed as a zero wrap angle experiment using a linear reciprocating tribometer [6,7]. By design, these experiments provide a more fundamental measurement of friction coefficient because the sample geometry is uniform and consistent. It represents a limiting case for the bushings and approximates a point contact without an infinite stress singularity. In these tribometers like the previously described bushing tribometer, the pin sample is mounted directly to a multi-axis load cell, assuring that the only force path from the contact to ground was through the load cell. Two standard samples of PTFE were machined from the same bushing stock and tested in the same orientation against a 304 stainless steel counterface with similar surface characteristics (Ra ~ 50 nm with random orientation) to the shafts. Following the same protocol as the evolving contact wrap angle experiments, an initial conditioning test was run for 20 m, where the pin was replaced and the test sample was run for 70 m. The contact pressure of reciprocating pin-on-flat testing was held constant at 6 MPa and sliding speed was 10 mm/s.

5. Results and discussion

5.1. Variable edge geometry

Friction coefficient is plotted versus sliding distance for two nominally identical standard bushings (sharp edges) in Fig. 6A. In the first experiment, the initial friction coefficient was $\mu = 0.27$ indicating failure of the coating. In the repeat experiment, the friction

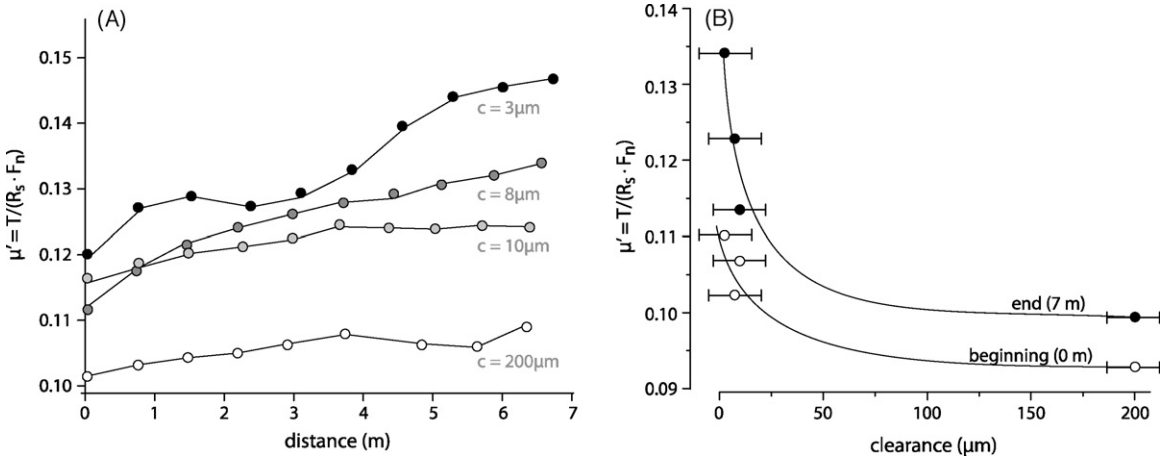

Fig. 7. (A) μ' plotted versus sliding distance for variable clearance experiments with UHMWPE bushings. (B) μ' plotted versus bushing clearance for the beginning and end of each experiment. Smaller clearances produced consistently higher torques.

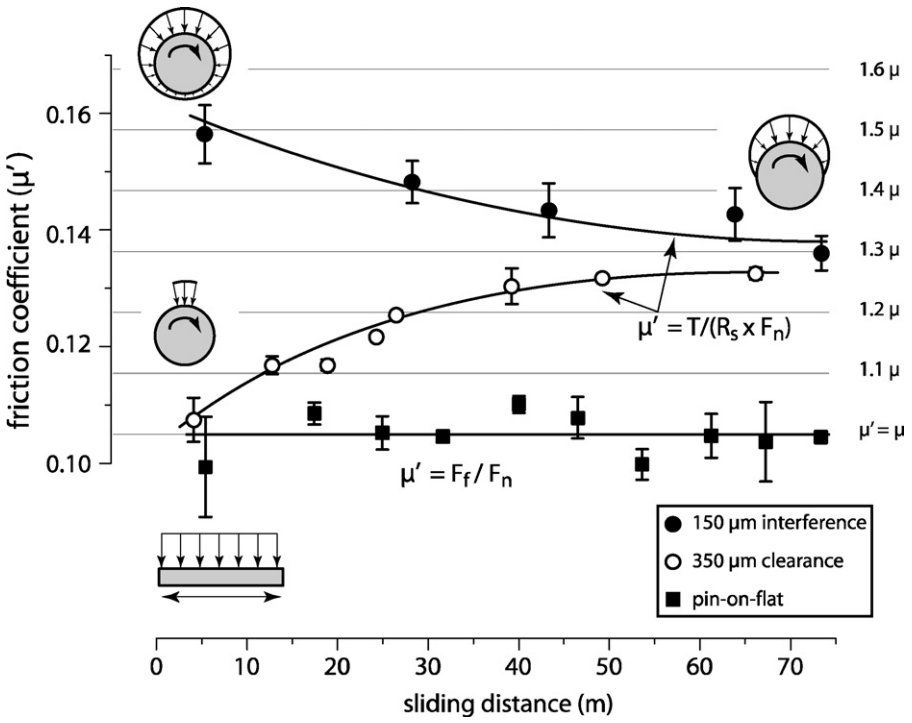

Fig. 8. Friction coefficient measurements plotted versus sliding distance for PTFE at a sliding speed of 10 mm/s. Data from clearance and interference bushings are compared to friction coefficient measurements of PTFE in a pin-on-flat contact geometry under comparable conditions. Friction coefficients of bushing experiments are calculated as the ratio of torque to the product of shaft radius and normal load. At steady state, the bushing friction coefficients approach the predicted value of 1.25 times the true friction coefficient as measured in pin-on-flat geometry.

coefficient started low and decreased during testing until the lubricant was exhausted and failure occurred after only 1000 sliding cycles.

Interrogation of the wear scars revealed that the severe contrast in the behaviors of nominally identical samples resulted from concentrated loading that likely occurred from slight sample to sample differences in bushing and shaft axis misalignments. The first sample had a thin wear scar at the edge of the bushing that concentrated the load at one edge and led to immediate failure of the film and steel on steel contact. Friction decreased as the wear scar spread momentarily bringing pristine areas of the coating into contact. The cycling between low and high friction continued until complete failure occurred at about 15 m. The wear scar of the second bushing was biased toward one edge, but to a lesser extent. Severe sensitivity of the system to misalignment is suggested by the fact that only the precision machined shafts and bushings were different.

The chamfered and radiused bushings were tested under the same conditions and showed substantially improved performance, so much so that Fig. 6B shows cycles to failure versus friction coefficient for all of the bushings. The two standard bushings, despite having a three order of magnitude difference in wear life, have almost negligible wear lives in comparison to the edge-modified bushings. The chamfered bushing failed after 35,000 sliding cycles and the radiused bushing ran for 60,000 cycles without failing at which point the experiments were halted. Over-constraints are inevitable in application and edge modification is clearly important in mitigating adverse effects of potential misalignments.

5.2. Variable clearances and geometric evolution

Values of μ' are plotted versus sliding distance for UHMWPE bushings with variable clearance in Fig. 7A. Values of μ' are plotted versus clearance at the beginning and end of the test in Fig. 7B. Samples with smaller clearances consistently had higher frictional torques than samples with larger clearances; the initial differences are consistent with the design chart in Appendix B. As sliding distance increased, the frictional torques in each case increased. Given the short test duration, and low sensitivity of torque to wrap angle at small angles, it is unlikely that the increase in torque at 200 μm clearance was due to geometric change from wear or creep; the change is likely due to run-in and a change in the value of the friction coefficient. Unlike PTFE, UHMWPE does not form beneficial transfer films and as a result the friction coefficient is often observed to vary significantly with sliding distance. Although variation in friction coefficient makes interpretation of the trend difficult, it is interesting that the dispersion between datasets increased as clearance reduced and sliding increased. The effects of wear and debris entrapments could cause such a trend.

The results of wear experiments with PTFE are shown in Fig. 8. The friction coefficient, as measured on a reciprocating pin-on-disk tribometer, was $\mu = 0.105 \pm 0.004$. As predicted by the model, the initial μ' for the 350 μm clearance system was only slightly higher than the friction coefficient. As the bushing wears, the mathematics indicate $\mu' = 1.25\,\mu = 0.131 \pm 0.004$. The 350 μm clearance data from Fig. 8 asymptotically approached this predicted limit. The deviation from smooth curvature is consistent with the observed deviations in the actual friction coefficient. The 150 μm interference system had an initial $\mu' = 1.6\mu$. The experimental data support the mathematical descriptions as μ' asymptotically decreased to the same limiting value of $\mu' = 1.25\mu$.

6. Conclusions

(1) A bushing tribometer was designed and constructed. The tribometer measures friction coefficients (μ') with low relative uncertainty and is capable of wide operating conditions that are application relevant.
(2) Misalignment sensitivity was studied. Relatively poor performance and large scatter in standard bushings were attributed to misalignment of shaft and bushing axes from inherent over-

constraint; a radius on the edge of the bushing mitigated these effects and increased wear life by several orders of magnitude.

(3) Clearance effects were investigated. Larger contact wrap angles were predicted to produce higher torques due to the presence of antagonistic force components that do not support the normal load. These effects were observed experimentally in clearance testing with UHMWPE of varying measured clearances. PTFE clearance and interference bushings wore rapidly and transitions to the same steady state value of friction coefficient were observed. These values were consistent with calculation based on friction coefficient measurements made using a linear reciprocating tribometer.

Acknowledgements

This material is based upon an AFOSR-MURI grant FA9550-04-1-0367. Any opinions, findings, and conclusions or recommendations expressed in this material are those of the authors and do not necessarily reflect the views of the Air Force Office of Scientific Research.

Appendix A.

A.1. Pressure distribution at steady state and T^* cosinusoidal pressure

A shaft is shown wearing into a bushing at steady state in Fig. A1A; the circular shaft penetrates into the entire bushing diameter (in the direction of the applied force) by an amount δ_0. Based on the wear rate equation, $k = \delta/(P{\cdot}D)$, the penetration depth is related to the maximum pressure through Eq. (A1):

$$\delta_0 = kP_0D \tag{A1}$$

where P_0 is the pressure at $\theta = 0$ and D is the sliding distance. At an arbitrary angle, θ, the wear depth is similarly related to P_θ, as shown in Eq. (A2):

$$\delta_\theta = kP_\theta D \tag{A2}$$

The trigonometric relationship between δ_θ and δ_0 is given by Eq. (A3):

$$\delta_\theta = \delta_0 \cos(\theta) \tag{A3}$$

Substituting Eqs. (A3) and (A1) into Eq. (A3) gives:

$$\delta_0 \cos(\theta) = kP_0D \cos(\theta) = kP_\theta D \tag{A4}$$

From Eq. (A4), it is clear that at steady state, $P_\theta = P_0 \cos(\theta)$.

The pressure distributions in real bushing systems are unknown. A reasonable approximation of a generic pressure distribution is the cosinusoidal pressure distribution depicted in Fig. A1B which follows the functional form of Eq. (A5).

$$P_\theta = P_{\max} \cdot \cos\left(\frac{\pi\theta}{2\alpha}\right) \tag{A5}$$

Inserting Eq. (A1) into Eq. (4) of the text, gives:

$$T^* = \frac{\int_0^\alpha P_\theta \, d\theta}{\int_0^\alpha P_\theta \cos(\theta)\, d\theta} = \frac{P_{\max}\int_0^\alpha \cos(\pi\theta/2\alpha)\, d\theta}{P_{\max}\int_0^\alpha \cos(\pi\theta/2\alpha)\cos(\theta) d\theta}$$
$$= \frac{\pi^2 - 4\alpha^2}{\pi^2 \cos(\alpha)} \tag{A6}$$

Appendix B.

B.1. Dependence of T^* and μ^* on clearance, force, and stiffness

The displacement, $\delta_{(\theta)}$, of the shaft into the bushing can be found using Eq. (B1). The shaft is assumed to be a rigid body compared to the bushing material. In this equation R_s is the radius of the shaft, R_b is the inner radius of the bushing and e is the eccentricity length between the shaft centers. The radial clearance is defined as $c = R_b - R_s$. The angle θ is measured from the line of eccentricity, which is assumed to be along the line of loading:

$$\delta_{(\theta)} = R_s - \sqrt{R_b^2 - e^2 \ \sin^2(\theta)} + e\cos(\theta) \tag{B1}$$

The pressure, $P_{(\theta)}$, at any angular location θ is calculated using a Winkler model for the polymeric bushing, Eq. (B2). The shaft normal vectors are used to define the line of action for the contact pressures along the region of positive displacement, $\theta_{\min} < \theta < \theta_{\max}$. For this analysis it is assumed that $2\theta < \pi$. The thickness of the bushing is defined as t and the effective modulus is given in Eq. (B3):

$$P_{(\theta)} = \frac{E'\delta_{(\theta)}}{t} \tag{B2}$$

$$E' = \frac{(1-\nu)E}{(1+\nu)(1-2\nu)} \tag{B3}$$

The normal load, F_n, supported over any symmetrical arc of interference defined by $\theta_{\max} = |\theta_{\min}| = \theta_m$ is given by the integral expression

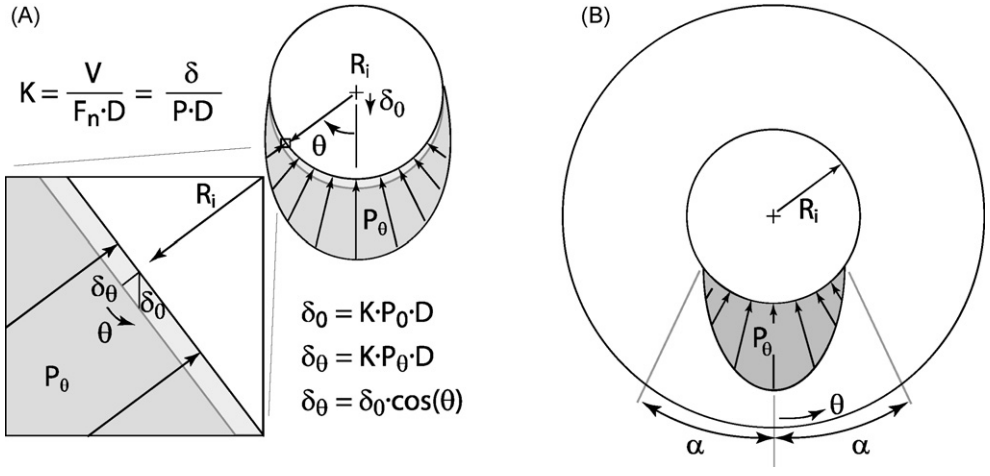

Fig. A1. Cosinusoidal pressure distribution.

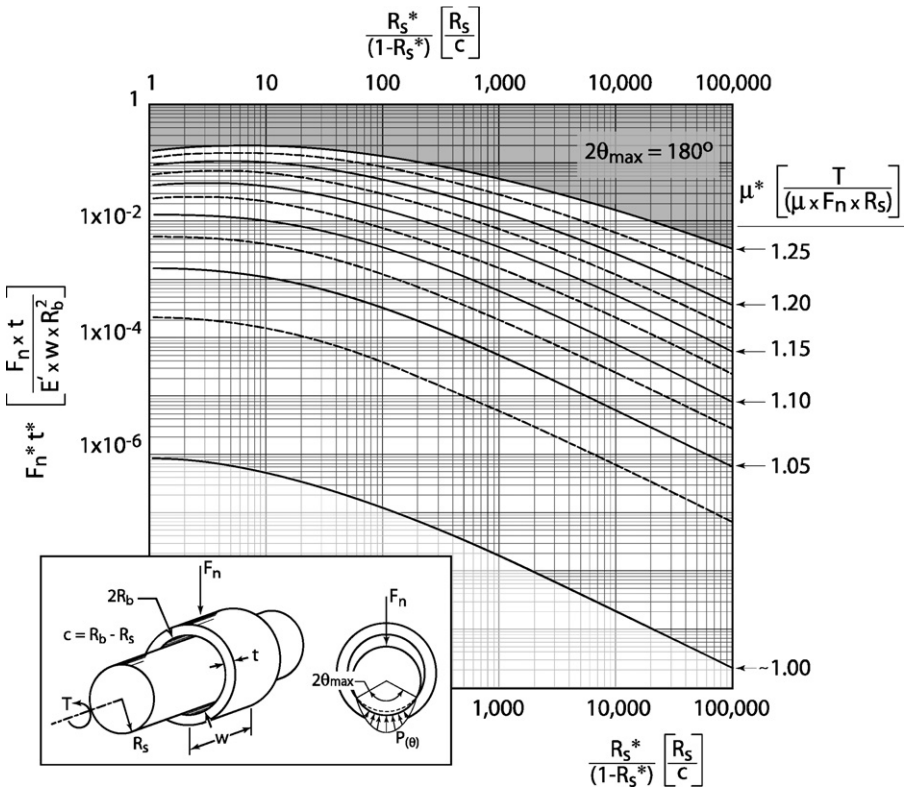

Fig. B1. A contour map illustrating the differences between the calculated frictional torque and expected values of torque based on applied load, friction coefficient, and shaft radius. There are strong effects from increased dimensionless load, increased dimensionless bushing thickness, and reduced normalized radial clearance.

shown in Eq. (B4), where w is the length of the bushing:

$$F_n = \int_{-\theta_m}^{\theta_m} P_{(\theta)} \cos(\theta) w R_s \, d\theta \tag{B4}$$

Assuming a friction coefficient of μ acts over entire area of contact, the frictional torque, T, generated in such a contact is given by Eq. (B5):

$$T = \int_{-\theta_m}^{\theta_m} \mu P_{(\theta)} \, w R_s^2 \, d\theta \tag{B5}$$

The measured friction coefficient, μ', is defined as the ratio of the frictional torque to the product of the applied load and shaft radius as discussed in the text; this is given in Eq. (B6):

$$\mu' = \frac{T}{F_n R_s} \tag{B6}$$

The normalized friction coefficient, μ^*, is defined as the ratio of the measured friction coefficient, μ', to the actual friction coefficient, μ, which is used in the calculation of torque, Eq. (B5). This ratio is always greater than unity because the antagonistic differential forces, $P_{(\theta)} \sin(\theta) \, dA$, do not contribute to the normal load but do contribute to the frictional torque. The equations can be represented in dimensionless form following the dimensionless variables and groups defined in Eqs. (B7)–(B10):

$$F_n^* = \frac{F_n}{E' R_b \, w} \tag{B7}$$

$$R_s^* = \frac{R_s}{R_b} \tag{B8}$$

$$t^* = \frac{t}{R_b} \tag{B9}$$

$$e^* = \frac{e}{R_b} = \sqrt{1 - R_s^{*2} \sin^2(\theta_m)} - R_s^* \cos(\theta_m) \tag{B10}$$

Fig. B1 shows a contour plot of the dimensionless friction coefficient, which is a normalized error between the calculated frictional torque and the expected frictional torque. The horizontal axis is a ratio of the shaft radius and the radial clearance. The vertical axis is the product of the normalized load and the bushing thickness. High values of this product are expected to result in larger arcs of contact.

References

[1] M. Mosleh, N. Saka, N.P. Suh, A mechanism of high friction in dry sliding bearings, Wear 252 (2002) 1–8.
[2] W.R. Jones Jr., M.J. Jansen, in: NASA (Ed.), Space Tribology, 2000, pp. 1–33.
[3] W.R. Jones Jr., S.V. Pepper, M.J. Jansen, Q.N. Nguyen, E.P. Kingsbury, S.H. Loewenthal, R.E. Predmore, A new apparatus to evaluate lubricants for space applications—the spiral orbit tribometer (sot), NASA (2000) 1–7.
[4] G. Stachowiak, A. Batchelor, Engineering Tribology, second ed., Butterworth–Heinemann, 2001.
[5] J.A. Williams, Engineering Tribology, Cambridge University Press, 2005, p. 488.
[6] T. Schmitz, J. Action, D. Burris, J. Ziegert, W. Sawyer, Wear-rate uncertainty analysis, ASME Journal of Tribology 126 (2004) 802–808.
[7] T. Schmitz, J. Action, J. Ziegert, W. Sawyer, The difficulty of measuring low friction: uncertainty analysis for friction coefficient measurements, ASME Journal of Tribology 127 (2005) 673–678.
[8] D.L. Burris, W.G. Sawyer, Addressing practical challenges of low friction coefficient measurements, Tribology Letters 35 (2009) 17–23.
[9] N.H. Kim, D.K. Won, D. Burris, B. Holtkamp, G.R. Gessel, P. Swanson, W.G. Sawyer, Finite element analysis and experiments of metal/metal wear in oscillatory contacts, Wear 258 (2005) 1787–1793.
[10] M.A. Hamilton, M.C. Sucec, B.J. Fregly, S.A. Banks, W.G. Sawyer, Quantifying multidirectional sliding motions in total knee replacements, ASME Journal of Tribology 127 (2005) 280–286.
[11] A. Wang, A unified theory of wear for ultra-high molecular weight polyethylene in multi-directional sliding, Wear 248 (2001) 38–47.
[12] D. Dickrell, D. Dooner, W.G. Sawyer, The evolution of geometry for a wearing circular cam: analytical and computer simulation with comparison to experiment, ASME Journal of Tribology 125 (2003) 187–192.

[13] D. Dickrell, W.G. Sawyer, Evolution of wear in a two-dimensional bushing, Tribology Transactions 47 (2004) 257–262.
[14] D. Burris, W. Sawyer, A low friction and ultra low wear rate peek/ptfe composite, Wear 261 (2006) 410–418.
[15] D.L. Burris, B. Boesl, G.R. Bourne, W.G. Sawyer, Polymeric nanocomposites for tribological applications, Macromolecular Materials and Engineering 292 (2007) 387–402.
[16] I. Jang, D.L. Burris, P.L. Dickrell, P.R. Barry, C. Santos, S.S. Perry, S.R. Phillpot, S.B. Sinnott, W.G. Sawyer, Sliding orientation effects on the tribological properties of polytetrafluoroethylene, Journal of Applied Physics 102 (2007).